



## Ni-based hydrotalcite-derived catalysts for enhanced CO<sub>2</sub> methanation: Thermal tuning of the metal-support interaction

Jie Ren <sup>a,\*</sup>, Han Lei <sup>b,1</sup>, Chalachew Mebrahtu <sup>c</sup>, Feng Zeng <sup>d</sup>, Xusheng Zheng <sup>e</sup>, Gang Pei <sup>a</sup>, Wenhua Zhang <sup>b,\*</sup>, Zhandong Wang <sup>e,\*</sup>

<sup>a</sup> Department of Thermal Science and Energy Engineering, University of Science and Technology of China, Hefei 230026, Anhui, China

<sup>b</sup> Hefei National Laboratory for Physical Sciences at the Microscale, University of Science and Technology of China, Hefei 230026, China

<sup>c</sup> Chair of Heterogeneous Catalysis and Chemical Technology, Institute for Technical and Macromolecular Chemistry, RWTH Aachen University, Worringerweg 2, 52074 Aachen, Germany

<sup>d</sup> State Key Laboratory of Materials-Oriented Chemical Engineering, College of Chemical Engineering, Nanjing Tech University, Nanjing 211816, Jiangsu, China

<sup>e</sup> National Synchrotron Radiation Laboratory, University of Science and Technology of China, Hefei 230026, Anhui, China



### ARTICLE INFO

#### Keywords:

CO<sub>2</sub> methanation  
Metal-support interaction  
Ni-based hydrotalcite-derived catalyst  
Thermal treatment  
DFT calculation

### ABSTRACT

Metal-support interaction (MSI) is recognized as an important factor affecting catalyst activity in CO<sub>2</sub> methanation, but a feasible strategy to adjust MSI during catalyst preparation is not yet very clear. Herein, we designed a series of Mg-Al hydrotalcites calcined at different temperatures as supports for Ni-based catalysts preparation and investigated the relationship between MSI and catalytic activity. Through various characterizations, it is confirmed that the MSI can be tailored by thermal treatment resulting from phase transformation, and Ni/MAO1000 (which has strong MSI) showed the highest activity for CO<sub>2</sub> conversion (1821 mmolCO<sub>2</sub> mol<sup>-1</sup> Ni min<sup>-1</sup>). Furthermore, in-situ DRIFTS experiments and DFT calculations proved that methoxy/carbonyls are key intermediates and Ni(111) is the determined crystal plane to produce CH<sub>4</sub>. This work provides an effective way to tailor the MSI of Ni-based catalysts for enhanced performance in CO<sub>2</sub> methanation.

### 1. Introduction

In recent years, with the development of power-to-gas technology, fuel production from renewable energy has attracted tremendous interest from industry and academia [1,2]. Combined with the green H<sub>2</sub> produced from water electrolysis during the power-to-gas process, CO<sub>2</sub> methanation is a promising approach to reduce environmental issues like global warming. As CO<sub>2</sub> methanation is a thermodynamically favored and kinetically limited reaction, an effective catalyst is required for this exothermic reaction [3,4]. With the characteristics of high activity and cheap price, Ni-based catalysts have been extensively studied for CO<sub>2</sub> methanation. Nevertheless, the continuous formation of Ni carbonyl species and byproducts such as CO and H<sub>2</sub>O could affect catalyst stability and even lead to catalyst deactivation [5,6]. Besides, although some Ni-based catalysts (e.g., commercial Ni/Al<sub>2</sub>O<sub>3</sub>) exhibited high activity for CO<sub>2</sub> methanation at high temperatures, carbon deposition and metal sintering facilitate its deactivation under reaction conditions.

Until now, many metal oxides have been used as supports (e.g., ZrO<sub>2</sub>, CeO<sub>2</sub>, and Al<sub>2</sub>O<sub>3</sub>) for Ni-based catalyst preparation, and the designed Ni-based catalysts exhibited a certain activity in CO<sub>2</sub> methanation [6,7]. Among these, Mg-Al hydrotalcite ([M<sub>1-x</sub><sup>2+</sup>M<sub>x</sub><sup>3+</sup>(OH)<sub>2</sub>](A<sup>n-</sup>)<sub>x/n</sub>·mH<sub>2</sub>O) with a thermally stable structure can form homogeneously mixed-metal oxides after calcination, which therefore attracts increasing attention as a potential candidate for the dispersion of active metals [8–10]. For instance, Abate et al. [11] observed 86% of CO<sub>2</sub> conversion and found the superior performance of the optimized catalyst (Ni-Al hydrotalcite prepared under a pH of 12 and 75% Ni loading) was attributed to the higher metal surface area (51.8 m<sup>2</sup>/g<sub>cat</sub>) and metal dispersion (16%). Moreover, Lewis basic promoters like MgO are able to prohibit carbon formation and are in favor of carbon gasification due to their excellent CO<sub>2</sub> adsorption capability [9]. Aiming at enhancing the stability of Ni-Al hydrotalcite-derived catalysts, we previously fabricated a series of Ni-Mg-Al hydrotalcites with different morphologies and applied them for CO<sub>2</sub> methanation [12]. It was observed that optimized Ni/Mg-Al hydrotalcite with a “rosette-like” structure and a strong metal-support

\* Corresponding authors.

E-mail addresses: [renchemie@hotmail.com](mailto:renchemie@hotmail.com) (J. Ren), [whhzhang@ustc.edu.cn](mailto:whhzhang@ustc.edu.cn) (W. Zhang), [zhdwang@ustc.edu.cn](mailto:zhdwang@ustc.edu.cn) (Z. Wang).

<sup>1</sup> These authors contributed equally to this work.

interaction (MSI) led to high basicity, optimized pore size, high Ni dispersion, high exposed metallic surface area, and therefore exhibited the highest CO<sub>2</sub> conversion and long-term stability (>120 h) during CO<sub>2</sub> methanation. In general, the activity of supported catalysts is significantly affected by the MSI between the support and the metallic sites which sensitively depends on the nature of the support, the electronic environment of active metal, and the pretreatment conditions employed [13–15]. For example, Lin et al. [16] applied reduction–oxidation cycles to regulate the MSI of Ni/CeO<sub>2</sub> catalyst, and catalytic activity was improved resulting from highly dispersed Ni particles, high density of oxygen vacancies, and high amount of weak basic sites during CO<sub>2</sub> methanation. Parastaev et al. [17] also controlled the particle size of Co/CeO<sub>2</sub>–ZrO<sub>2</sub> through high-temperature treatment and found a boosted catalytic performance due to the existence of oxygen vacancies and hydrogen spillover in the catalyst with large particle size support. Pu et al. [18] designed a series of Ni/CeO<sub>2</sub> catalysts through various complicated methods, and they demonstrated that the encapsulation degree of Ni particles (originating from the strong MSI effect) affected the CO<sub>2</sub> hydrogenation activity. Moreover, Shen et al. controlled the calcination temperature of support (i.e., hydrotalcite) to support Pd and In, and they proved the enhanced MSI was responsible for their activity in propane dehydrogenation [19]. All the above-mentioned results demonstrated that tailored MSI could enhance the catalyst activity in CO<sub>2</sub> methanation but controlling the MSI of catalysts seems to be complicated (possibly tailored by preparation method and addition of promoters). More importantly, an updated study on the feasible synthesis of Ni-based catalysts with weak as well as strong MSI and their direct effect on the surface morphology, particle size, basicity, and pore structure as well as their potential influence on the reaction mechanisms are rarely reported.

Hence, in the present work, we shared a facile method to tailor MSI of Ni-based catalysts over Mg-Al hydrotalcites (Ni/MAO) by thermal tuning of the particle size and support state. Through various characterizations such as XRD, HR-TEM, SEM, XPS, and XAS, we found that the 10 wt% Ni over Mg-Al hydrotalcites calcined at high temperature possessed the smallest particle size, high Ni dispersion, high basic sites, and strong MSI, thus exhibiting excellent activity and stability in CO<sub>2</sub> methanation. In addition, combining the in-situ DRIFTS with DFT results, CO<sub>2</sub> methanation mechanisms over the designed catalysts are proposed and the rate-determining step (RDS) among the intermediates conversion is investigated. Finally, we believe that the results obtained and perspectives of this work provide a strategy to rationalize future catalytic design and development for CO<sub>2</sub> methanation.

## 2. Experimental section

### 2.1. Support and catalyst preparation

(Mg, Al)O<sub>x</sub> (MAO) was fabricated by a co-precipitation method, and MAO precursors calcined at 500, 600, 800, and 1000 °C were named as MAO500, MAO600, MAO800, and MAO1000, respectively. After that, Ni/MAO catalysts were prepared by an incipient wetness impregnation method, and Ni loading of catalysts was controlled at 10 wt%. The obtained catalysts were denoted as Ni/MAO500, Ni/MAO600, Ni/MAO800, and Ni/MAO1000, respectively. The details can be found in the [Supporting information](#).

### 2.2. Catalyst characterization

X-ray diffraction (XRD) patterns were recorded using a Bruker D8 ADVANCE with Cu K $\alpha$  radiation at 40 kV and 30 mA. The pore structure and characteristics of samples were determined by means of a Quantachrome Autosorb-1 instrument. H<sub>2</sub> temperature-programmed reduction (H<sub>2</sub>-TPR) was conducted in a ChemBET Pulsar TPR/TPD automated chemisorption analyzer to determine the reducibility of the calcined Ni/MAO. The total basicity and basic sites distribution of the samples was

calculated using CO<sub>2</sub>-temperature-programmed desorption (CO<sub>2</sub>-TPD). The morphologies of supports and catalysts were investigated on a GeminiSEM 500. Ni particle size distribution of the reduced Ni/MAO catalysts was studied by transmission electron microscopy (TEM, FEI Tecnai F20 microscope equipped with a high-angle annular dark-field detector (HAADF)), and digital micrograph software was used to measure the inter-planar distances and structural defects. Ni content of the synthesized samples was quantified using an inductively coupled plasma atomic emission spectrometer (ICP—OES, Agilent 8800 ICP—MS). X-ray photoelectron spectroscopy (XPS) was employed with an Al K $\alpha$  radiation X-ray source in Thermo ESCALAB 250Xi for analyzing the chemical state of reduced catalysts, and XPSpeak41 software was applied for data analysis. Soft X-ray adsorption (sXAS) measurements were performed at the photoemission end-station at beamline BL10B of National Synchrotron Radiation Laboratory (NSRL) in Hefei, China. In addition, to unravel the methanation pathway over the designed catalysts, in-situ DRIFTS experiments were performed using a Nicolet iS50 spectrometer equipped with an in-situ diffuse reflectance cell with a high-temperature reaction chamber (Praying Mantis™, Harrick), and mercury cadmium telluride (MCT) detector. The detailed instruments and procedures are presented in [Supporting information](#).

### 2.3. Methanation test

The catalytic CO<sub>2</sub> methanation were performed using a fixed bed continuous flow reactor equipped with a quartz tubular reactor with an 8 mm internal diameter. The calcined Ni/MAO catalysts (100 mg, 180–250  $\mu$ m particle size) diluted with 600 mg sand was loaded into the reactor, and the methanation was carried out at 200–500 °C after in-situ reduction. An online PANNA A60 gas chromatograph equipped with thermal conductivity detector (TCD) is used to analyze the products. The detailed procedures, gas feed mixture, calculation for CO<sub>2</sub> conversion rate and CH<sub>4</sub> selectivity are given in [Supporting information](#).

### 2.4. Computational details

All the energy calculations were performed in Vienna Ab initio Simulation Package (VASP) within the projector augmented wave (PAW) method [20,21]. The Perdew-Burke-Ernzerhof (PBE) general gradient approximation (GGA) functional is employed [22]. The cutoff energy for the plane-wave basis was 400 eV. The integration in the Brillouin zone was set to  $3 \times 3 \times 1$  for Ni(110) and Ni(111), and a  $2 \times 2 \times 1$  *k*-point grid was used for composite catalysts sampled by the Monkhorst-Pack scheme [23]. DFT-D2 was used to describe the van der Waals interaction [24]. The energy convergence criteria and force tolerance were set as 10–5 eV $\text{\AA}^{-1}$  per unit cell and 0.03 eV $\text{\AA}^{-1}$  respectively [25]. The vacuum region of 15 Å was used to avoid the interactions between slabs in the *z* axis. The reaction transition states (TS) were adopting the climbing image nudged elastic band method (CI-NEB) [26]. The p(3 $\times$ 2) surface of Ni(110) with six atomic layers and p(2 $\times$ 2) surface of Ni(111) with four atomic layers were constructed to simulate pure Ni catalyst. The p(3 $\times$ 2) surface of MgO(110), p(2 $\times$ 1) surface of Al<sub>2</sub>O<sub>3</sub>(110) and p(2 $\times$ 2) surface of MgAl<sub>2</sub>O<sub>4</sub>(110) were used to the substrates, the lattice mismatch rate between the substrates and Ni cluster is within 5 %. The bottom half of the atomic layer was fixed in pure Ni model, whereas only half of the atomic layer of the substrate is fixed, and the supported Ni clusters were completely relaxed in the composite catalysts.

## 3. Results and discussion

### 3.1. Characterization of supports and catalysts

A series of MAO (i.e., (Mg, Al)O<sub>x</sub>) and Ni/MAO (i.e., Ni/(Mg, Al)O<sub>x</sub>) catalysts with 10 wt% of Ni loading were synthesized by co-precipitation to obtain Mg-Al hydrotalcites and incipient wetness impregnation to

load Ni (the details of catalyst synthesis are presented in **Fig. S1** of the **Supporting information**). The formation and evolution of spinel structure (i.e.,  $\text{MgAl}_2\text{O}_4$ ) derived from Mg-Al hydrotalcites through temperature treatment was first confirmed by XRD characterization (**Fig. S2**) [27]. Besides, as shown in **Fig. S2**, with the addition of Ni, formation metallic Ni ( $\text{Ni}^0$ ) was only detected in the Ni supported on Mg-Al hydrotalcite without calcination (Ni/MAOr), which indicated that the highly dispersed Ni was retained over other Ni/MAO catalysts. Additionally, it is found that the formed  $\text{MgAl}_2\text{O}_4$  coexisted with  $\text{MgO}$  in the samples treated at high temperature, and a distinct  $\text{Al}_2\text{O}_3$  reflex is not detected in all the prepared samples. Furthermore, the textual properties of supports and catalysts were analyzed by  $\text{N}_2$  physisorption, and results are presented in **supporting information**. It is observed that temperature treatment will cause a decrease in specific surface area and total pore volume of samples.

It has been widely reported that the MSI plays a crucial role in tuning the catalytic efficiency of supported metal active sites [28,29], and  $\text{H}_2$ -TPR is an important characterization method to investigate the reduction behavior of the active metal and strength of its MSI. As shown in **Fig. S4**, in addition to Ni/MAO1000, Ni supported on Mg-Al hydrotalcites calcined at higher calcination temperatures possessed a higher content of  $\gamma$ -type  $\text{NiO}$  (i.e.,  $\text{NiO}$  phase strongly interacted with the support). The literature has noted out that a strong MSI in catalysts alters the chemical state/structure of active phase, resulting in weaker adsorption of CO during  $\text{CO}_2$  methanation (i.e. CO is a key intermediate in the dissociative route of  $\text{CO}_2$  methanation) [30]. In addition, strong MSI in Ni-based catalysts inhibits  $\text{NiO}$  reduction at intermediate reduction temperatures, and this in turn results formation of less active H atoms during the  $\text{CO}_2$  methanation. As depicted in **Fig. S4** of the **supporting information**, the Ni/MAO1000 showed close reduction-temperature centers of the three type of  $\text{NiO}$  (relatively at lower temperature compared to the other catalysts) which indicates a good reductivity of this catalyst. Furthermore, the reduction degree (RD) of catalysts was calculated by relative area ratio (**eq. S1, supporting information**), and the highest RD (92.5 %) is obtained over the Ni/MAO1000 catalyst. The Ni dispersion of reduced catalysts was calculated and compared by TEM and CO pulse chemisorption, and the close results from both characterizations revealed Ni/MAO1000 with the highest Ni dispersion (19.0 %) may exhibit better activity for  $\text{H}_2$  dissociation and then for  $\text{CO}_2$  methanation.

To unravel the  $\text{CO}_2$  adsorption and desorption capacity, the basicity of Ni/MAO catalysts was determined by  $\text{CO}_2$ -TPD, and the results are presented in **Fig. S5** and **Table 1**. It can be observed that the fraction of weak (-OH groups) and medium ( $\text{Mg}^{2+}$ - $\text{O}^{2-}$  pairs) basic sites increase as calcination temperature increases. Besides, the peak temperature of weak basicity slightly shifted to a lower temperature with the increase of calcination temperature, indicating that the  $\text{CO}_2$  adsorbed on -OH groups was easy to desorb [27]. Interestingly, the medium basic sites are important for the adsorption of  $\text{CO}_2$  on the catalyst surface under the reaction conditions, and therefore Ni/MAO1000 with 1.14 mmol/g<sub>cat</sub> of medium basic sites is considered to adsorb and activate more  $\text{CO}_2$  molecules for hydrogenation.

With increasing calcination temperature, the nanosheet-type morphologies of both MAO and Ni/MAO (**Fig. 1b** and **c**, **Figs. S6** and **S7**) gradually become thinner, which in turn will result in an increased

specific surface area (**Fig. S3** and **Table S1**) as well as active sites per gram of catalyst and then make a prominent contribution to  $\text{CO}_2$  activation and hydrogenation. HR-TEM and EDX mapping of the Ni/MAO600 and Ni/MAO1000 are presented in **Fig. S8** and **Fig. 1d-f**. As can be seen, well-dispersed Ni nanoparticles over the catalyst support are obtained, especially, the Ni in Ni/MAO1000 is partially moved to the catalyst surface with the increase of calcination temperature (an increased MSI). The higher  $\text{MgAl}_2\text{O}_4$  content available in Ni/MAO1000 is believed to provide a strong MSI, which therefore led to the formation of more metallic sites and a preferable Ni crystal plane for  $\text{H}_2$  dissociation and then methanation. The Ni particle size of Ni/MAO600 and Ni/MAO1000 ranged from 1 nm to 11 nm, and Ni/MAO1000 with the smallest Ni particle size (6.1 nm, close to the results (**Table S1**) determined by CO pulse chemisorption) tends to exhibit higher intrinsic activity [31]. Besides, the selected area electron diffraction (SEAD) images of the catalysts revealed the high crystallinity and presence of both Ni (110) and Ni(111) crystal planes, which proved to play a key role in  $\text{H}_2$  adsorption and dissociation [32,33]. The surface chemical state of the representative catalyst (i.e., Ni/MAO600 and Ni/MAO1000) was confirmed by XPS, and the results are presented in **Fig. 2**.

The Ni  $2p_{3/2}$  spectra of reduced catalysts can be divided into three peaks, which are centered at  $\sim 852/869$  eV and  $\sim 855/873$  eV relating to  $\text{Ni}^0$  species and  $\text{Ni}^{2+}$ , respectively. In addition, a shake-up satellite peak of complex Ni at  $\sim 861/880$  eV can be also found in two catalysts [34,35]. In particular, it is observed that the binding energy of  $\text{Ni}^0$  in Ni/MAO1000 almost disappeared, which indicated the Ni/MAO1000 with small and dispersed Ni (due to the existence of stronger MSI) was easily oxidized during sample transfer. The recorded O 1s peak (**Fig. 2b**) of two catalysts were deconvoluted into two Gaussian curves (centered at around 529 eV and 531 eV), which attributed to lattice oxygen ( $\text{O}_{\text{lat.}}$ ) and defect oxygen ( $\text{O}_{\text{def.}}$ ) [35,36]. The intensity of  $\text{O}_{\text{def.}}$  in Ni/MAO1000 showed higher than of Ni/MAO600 due to the high temperature treatment of Ni/MAO1000. Besides, a slight shift of  $\text{O}_{\text{lat.}}$  to higher BE was observed, which could be explained as the formation and evolution of  $\text{MgAl}_2\text{O}_4$  spinel structure (consistent with XRD analysis).

Clear differences in the electronic environment were observed using soft X-ray absorption spectroscopy (sxAS), and the L-edge XAS spectra of Ni and O for the reduced Ni/MAO catalysts are presented in **Fig. 1g** and **Fig. S9**. It is evident from the spectrum that Ni L-edge spectra of catalysts, in which two typical  $\text{L}_2$  and  $\text{L}_3$  peaks are observed at about 853 eV and 872 eV, respectively. Obviously, with the increase of calcination temperature, both the  $\text{L}_2$  and  $\text{L}_3$  peaks of Ni in Ni/MAO catalysts experience a negative shift, which therefore demonstrates the enlarged electron density around the Ni atoms [37]. The enlarged electron density around  $\text{Ni}^0$  can be explained by the different interactions between support and Ni, among which, the signal of Ni/MAO1000 with a huge negative shift may expose more active sites for reaction. In comparison with the above analysis, the formation of  $\text{MgAl}_2\text{O}_4$  enhanced the MSI between  $\text{Ni}^0$  and support, which therefore promoted the  $\text{NiO}$  reduction. In addition, the position and shape of O K-edge in Ni/MAO catalysts proved the change in the oxygen environment, that is, the  $\text{MgAl}_2\text{O}_4$  formation originated from  $\text{Al}_2\text{O}_3$  and  $\text{MgO}$ .

### 3.2. Catalytic performance and mechanistic understanding

The catalytic activity of the as-prepared Ni/MAO catalysts was evaluated in  $\text{CO}_2$  methanation at temperatures between 200 and 500 °C under 1 atm with a stoichiometric  $\text{CO}_2/\text{H}_2$  ratio (16 %  $\text{CO}_2$ , 64 %  $\text{H}_2$ , and 20 %  $\text{N}_2$  for balance). As can be seen from **Fig. 3**, the overall activity over the Ni/MAO1000 catalyst is much higher than that of the other Ni/MAO catalysts during the whole temperature range, and a  $\text{CO}_2$  conversion rate of  $1821 \text{ mmolCO}_2 \text{ mol}^{-1} \text{ Ni min}^{-1}$  and a  $\text{CH}_4$  selectivity of 98.8 % are achieved over the Ni/MAO1000 catalyst at 400 °C. The gradually increased CO selectivity at higher temperatures over all catalysts was attributed to the occurrence of reverse water-gas shift reaction. In addition, Ni/MAOr (only thermally treated sample under reduction

**Table 1**  
Physicochemical characteristics of obtained Ni/MAOs.

Samples	Ni loading (wt %)	Ni dispersion (%)	RD (%)	Basic sites (mmol/g <sub>cat</sub> )
Ni/MAOr	10.1	10.2	88.6	2.48
Ni/MAO500	9.2	10.3	84.5	1.28
Ni/MAO600	9.3	11.0	85.7	1.48
Ni/MAO800	9.8	13.8	88.7	1.77
Ni/MAO1000	9.2	19.0	92.5	2.18

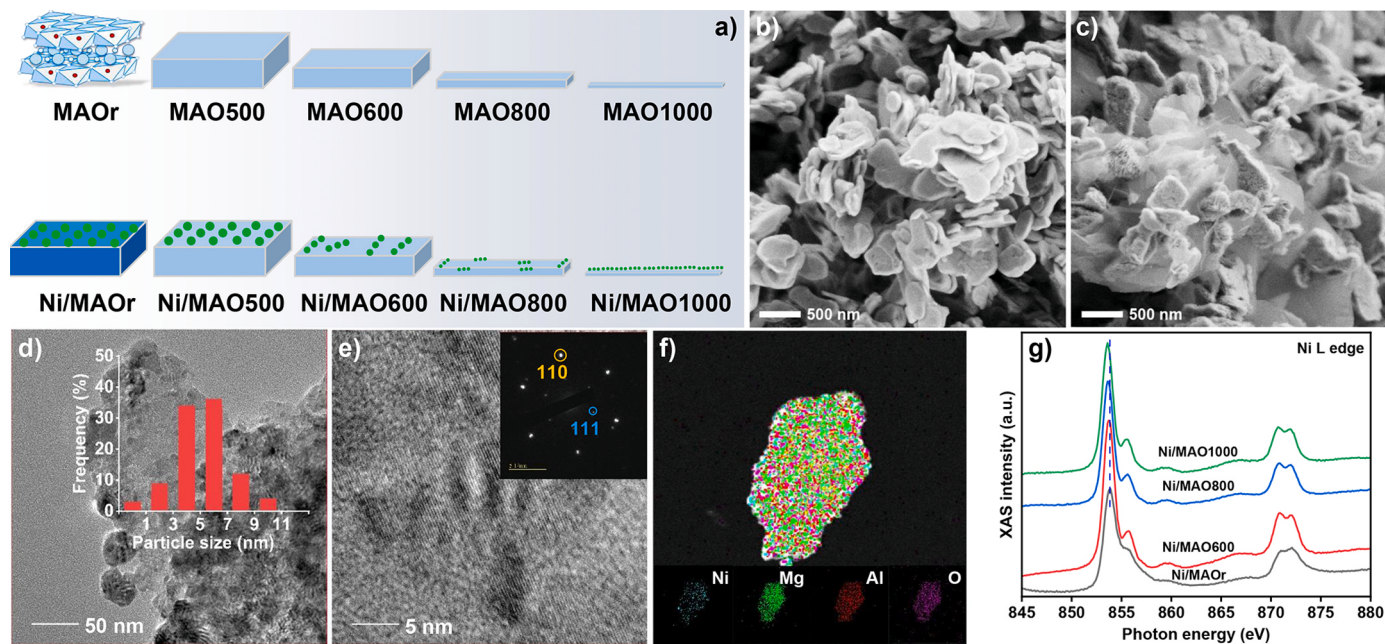


**Fig. 1.** (a) The formation pathway of MAOs and Ni/MAO catalysts. (b) SEM of calcined MAO1000. (c) SEM of calcined Ni/MAO1000. (d, e, and f) TEM image (inset: Ni particle size distribution), HR-TEM image (inset: SEAD image), and EDX mapping of reduced Ni/MAO1000 catalyst. (g) Ni L-edge spectra of Ni/MAO catalysts.

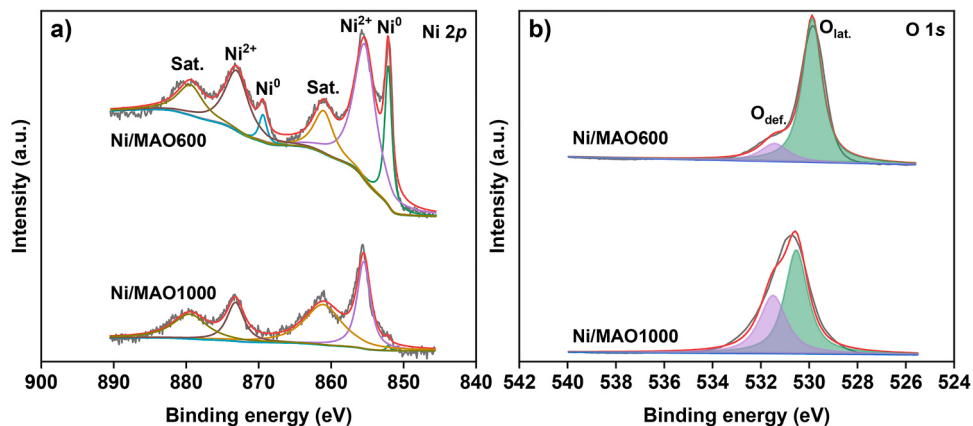


**Fig. 2.** (a) Ni 2p and (b) O 1s spectra of Ni/MAO600 and Ni/MAO1000 catalysts.

process) showed the lowest CO<sub>2</sub> conversion rate indicating the modification of the MSI even compared with Ni/MAO600 catalyst (Ni supported on the MAO which was calcined at low temperature).

As discussed in the characterization section, the metal dispersion and RD of Ni/MAO1000 are highest among all Ni/MAO catalysts. However, the high metal dispersion and RD normally induce the agglomeration of metal under high-temperature reaction and reduction conditions [38, 39]. Therefore, the stability experiments of representative Ni/MAO catalysts were performed. As shown in Fig. 3c, Ni/MAO1000 with a strong MSI is extremely stable during 100 h time on stream (TOS), which therefore prohibits deactivation of Ni due to oxidation and carbon deposition. In comparison, during the stability test, CO<sub>2</sub> conversion rate of Ni/MAOr decreased by 24.9 % after 100 h (Fig. 3c), and further confirming that the activity and stability of catalysts are significantly affected by the MAO pretreatment. The Ni dispersion of the spent catalysts was investigated by TEM (Fig. S10, supporting information), and the results revealed that the Ni particle size and dispersion of spent Ni/MAO600 and Ni/MAO1000 catalysts are maintained even after 100 h TOS. In contrast, agglomeration is observed over the Ni in Ni/MAOr catalyst (i.e. the catalyst without pretreatment during catalyst

preparation) is confirmed. Furthermore, the CO<sub>2</sub> conversion rate of the best performing catalyst (Ni/MAO1000) in this work is compared with literature data. As presented in Table S2, Ni-based catalysts reported in literature usually possess high Ni loading to reach the high CO<sub>2</sub> conversion, but the catalysts reported in this work (i.e., with relatively low Ni loading and optimized MSI) exhibited high activity for CO<sub>2</sub> methanation at lower reaction temperatures. The textual properties (e.g., morphology and specific surface area) of Mg-Al hydrotalcites are significantly influenced by temperature treatment, and this led to a change in chemical properties together with MSI of the prepared Ni-based catalysts. To have a clear understanding, RD and basic sites are correlated with as shown, CO<sub>2</sub> conversion rate in Fig. 3d. Accordingly, Ni/MAO1000 catalyst with an optimized MSI (based on the higher RD). Besides, the basic sites of the prepared catalysts increased with an increase of the support calcination temperature. Therefore, these higher reducibility and high basic sites of the Ni/MAO1000 catalyst facilitate the adsorption/activation of both H<sub>2</sub> and CO<sub>2</sub> to realize CO<sub>2</sub> methanation, which results in a CO<sub>2</sub> conversion rate of 1821 mmolCO<sub>2</sub> mol<sup>-1</sup> Ni min<sup>-1</sup> at 400 °C.

As suggested in the literature, there are two mechanisms in CO<sub>2</sub>

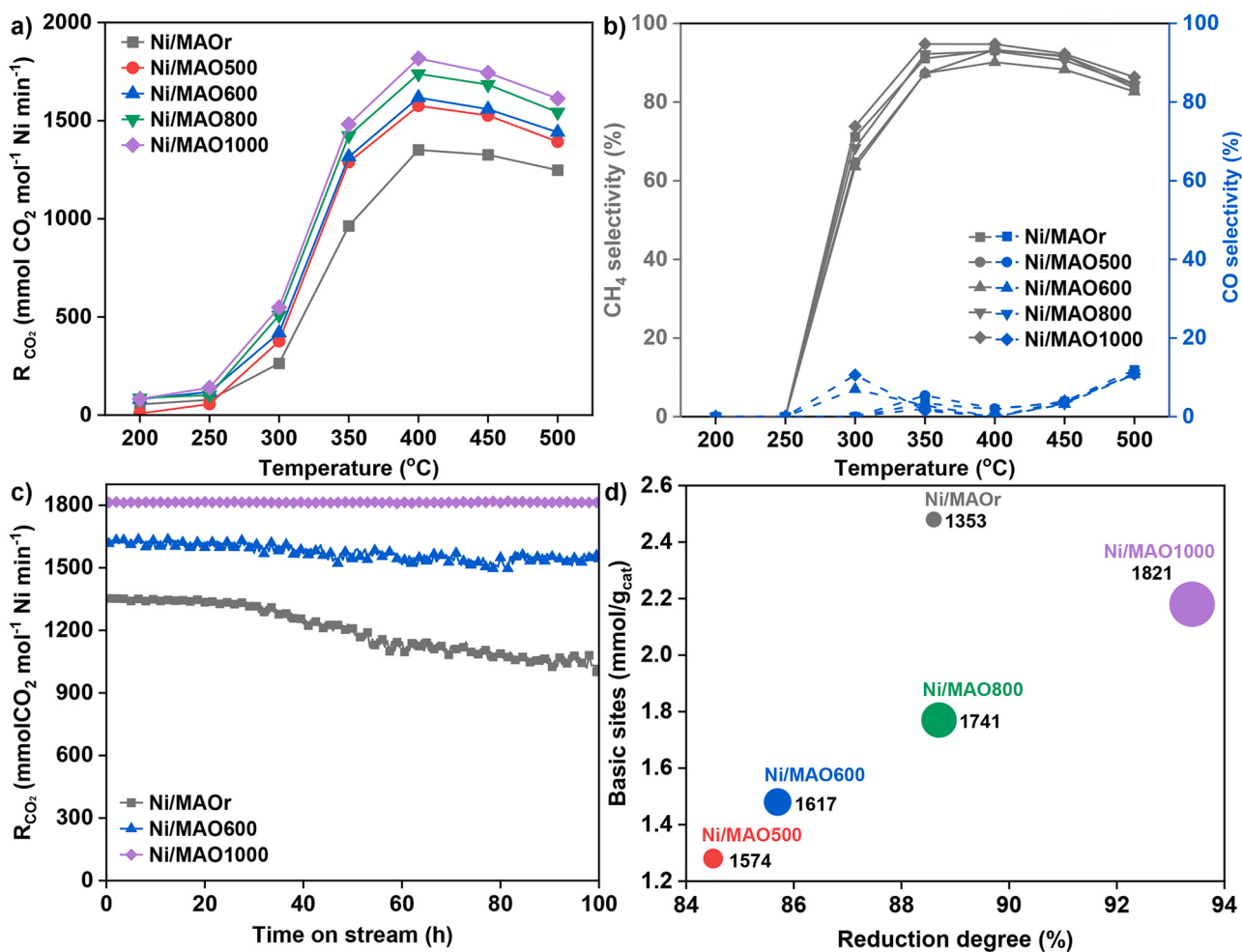


**Fig. 3.** (a) CO<sub>2</sub> conversion rate over Ni/MAO catalysts during CO<sub>2</sub> methanation. (b) CH<sub>4</sub> and CO selectivity over Ni/MAO catalysts during CO<sub>2</sub> methanation. (c) Stability of Ni/MAOr, Ni/MAO600, and Ni/MAO1000 catalysts during 100 h time on stream. (d) Correlation between reduction degree, basic sites and CO<sub>2</sub> conversion rate for CO<sub>2</sub> methanation at 400 °C.

methanation including associative (production of CH<sub>4</sub> without formation of CO as surface intermediate) and dissociative pathway (with the formation of CO as surface intermediate) [40,41]. In general, the CO<sub>2</sub> methanation pathway over Ni-based catalysts could be influenced by Ni particle size, electronic environment, and support type [42,43]. Therefore, in-situ DRIFTS experiments (CO<sub>2</sub> adsorption and methanation) were performed to reveal the catalytic mechanism over designed catalysts. As depicted in Fig. 4a, carbon-containing species adsorbed over the catalyst surface such as bicarbonates (\*HCO<sub>3</sub>), carboxylates (\*COOH), and carbonates (\*CO<sub>3</sub>) are identified at 1620, 1560, and 1440 cm<sup>-1</sup>, respectively. The presence of \*CO signals at 1900–2100 cm<sup>-1</sup> proved that dissociation of CO<sub>2</sub> to CO occurred over the catalyst surface especially on Ni(111) facets through CO<sub>2ad</sub> → CO<sub>ad</sub> + O<sub>ad</sub> [44], and the CO route has been explained as the superior path for methane formation. With the increasing calcination temperature of the catalyst support, it is observed that the strength of adsorbed species becomes higher indicating that Ni/MAO1000 with the strong MSI has a strong capacity for the adsorption and activation of CO<sub>2</sub>. To have a better understanding of the different reaction conditions, Ni/MAO1000 was selected as the optimum catalyst, and CO<sub>2</sub> adsorption and methanation experiments were performed in the temperature range of 200–500 °C. As shown in Fig. S11, the peak area of linear \*CO signal first increased and then strongly decreased between 50 and 500 °C, and a slight red shift from 2080 to 2070 cm<sup>-1</sup> is observed from 250 °C onwards. The red shift of the \*CO peak indicates the decrease in \*CO coverage and thereby a decrease in adjacent carbonyl-carbonyl interactions [45]. With

increasing temperature, the intensity of bidentate formate (\*HCOO) located at around 1703 cm<sup>-1</sup> is superior but the bidentate carbonates (\*HCO<sub>3</sub>) signal at around 1660 cm<sup>-1</sup> becomes weaker, which indicates the formation of formates should be involved at methanation temperatures. In-situ DRIFTS experiments for CO<sub>2</sub> methanation over Ni/MAO catalysts were conducted and obtained results are presented in Fig. 4b. As shown, the peak at around 3014 and 1302 cm<sup>-1</sup> could be ascribed to the C–H bonds of CH<sub>4</sub> [46,47], and the gradual increase in the peak intensity confirms that the catalyst achieves better activity at higher temperatures [48]. Interestingly, in addition to bidentate formate (\*HCOO) and \*CO, all carbon-containing species (mainly carbonates) disappeared, indicating the fast conversion of carbonates. To further understand the differences in the intermediates formed over various Ni/MAO catalysts, the peak intensity was semi-quantitatively calculated by Kubelka-Munk equation (Fig. 4c). As shown, with increasing calcination temperature of support during catalyst preparation, the \*CH<sub>4</sub> and \*HCOO peak intensity are enhanced. Also, the methanation route over the Ni/MAO catalyst could be governed by the formate step, and bidentate formate should be the key intermediate during the process. Based on the above in-situ DRIFTS results, the potential reaction pathways for CO<sub>2</sub> methanation over Ni/MAO catalysts are proposed in Fig. 4d. In principle, H<sub>2</sub> is dissociated to H atoms over the dispersed Ni, especially on Ni(111) plane, and gaseous CO<sub>2</sub> is adsorbed and reacts with surface OH groups and structural defects [49]. Afterward, the continued hydrogenation of bidentate bicarbonates (\*HCO<sub>3</sub>) (formate route), the deoxygenation of monodentate carbonates (\*CO<sub>3</sub>), and

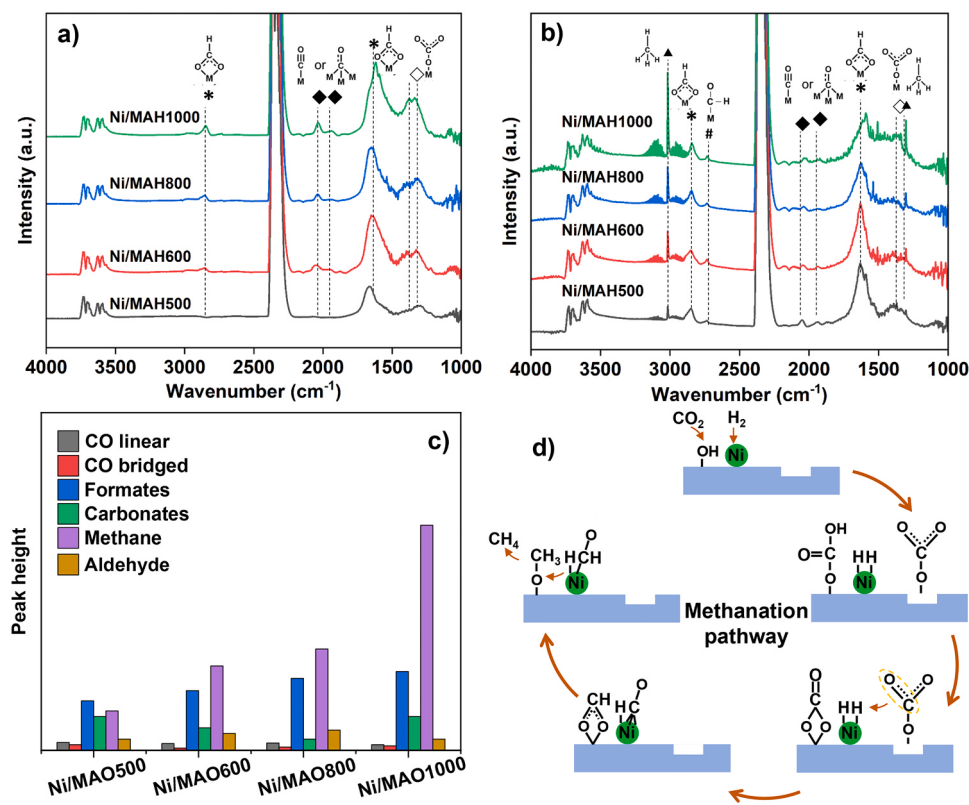


**Fig. 4.** (a and b) In situ DRIFT spectra of CO<sub>2</sub> adsorption and CO<sub>2</sub> methanation over Ni/MAO1000. (c) Relative quantification of the intermediates formed during in-situ DRIFTS experiments. (d) Proposed mechanism of CO<sub>2</sub> methanation over Ni/MAO catalysts.

hydrogenation of the stable bridged CO species (CO route) to form methane.

In order to fully understand the effect of MSI on the catalytic performance and reveal the reaction mechanism, density functional theory (DFT) calculations were also performed in detail. As MAO mainly consists of Al<sub>2</sub>O<sub>3</sub>, MgO, and Mg<sub>2</sub>A<sub>2</sub>O<sub>4</sub>, and the content of Mg<sub>2</sub>A<sub>2</sub>O<sub>4</sub> increases when the hydrotalcite precursor is calcined at a higher temperature, therefore, Al<sub>2</sub>O<sub>3</sub>(110), MgO(110) and Mg<sub>2</sub>A<sub>2</sub>O<sub>4</sub>(110) are used as supports of the Ni clusters to simulate the CO<sub>2</sub> methanation over the designed catalysts. In addition, to understand the preferred Ni plane for CO<sub>2</sub> hydrogenation, Ni(111) and Ni(110) are employed during the calculation. Then, the reaction mechanism of CO<sub>2</sub> methanation over these predefined catalyst surfaces (i.e., corresponding catalyst structures are shown in Fig. S12) is identified by DFT. The reaction pathway of CO<sub>2</sub> reduction proposed above has been identified and the reaction coordinate was calculated, from which we can find that the CO<sub>2</sub> is directly dissociated to CO\* on Ni(110) and CO\* subsequently tends to hydrogenate to CHO\* rather than desorption, but methanol is the main reduction product. The optimized structures are shown in Figs. S13-S16 and the corresponding energy diagrams are shown in Figs. S17-S19. The reduction of CO<sub>2</sub> on Ni(111) tends to obtain HCOO\*, and then hydrogenated to CH<sub>3</sub>O\* as the key intermediate, which largely determines the selectivity of products. CH<sub>4</sub> and CH<sub>3</sub>OH were achieved by breaking C-O bond and hydrogenation of CH<sub>3</sub>\*, respectively. All the intermediates that can potentially be formed on Ni(111) are shown in Figs. S20-S23. The optimal pathway for CH<sub>4</sub> formation on Ni(111) i.e., the relative energy diagram is shown in Fig. 5a. Accordingly, the energy barrier of CH<sub>3</sub>O\* dissociation which is the rate-determining step (RDS) is 1.26 eV but is lower than the energy barrier of CH<sub>3</sub>OH formation (1.59 eV). Therefore, the CH<sub>4</sub> selectivity on Ni(111) is higher than CH<sub>3</sub>OH, and the Ni/MAO1000 catalyst with abundant Ni(111) sites is considered to be the most active catalyst. Aiming at improved catalytic performance, the mechanisms on Ni<sub>c</sub>/MgO(110) (Ni<sub>c</sub> = Ni cluster) are also determined,

where CO<sub>2</sub> is hydrogenated to CH<sub>3</sub>O\* by the same pathway as of the Ni (111) surface (Fig. 5b). The energy barrier of CH<sub>3</sub>O\* dissociation on Ni<sub>c</sub>/MgO(110) is 1.03 eV. It is not only lower than the methanol formation energy barrier (1.13 eV), but also lower than the dissociation energy barrier on Ni(111) surfaces. This indicates the existence of an optimized MSI between MgO(110) and Ni cluster, which can further improve the catalytic activity in CO<sub>2</sub> methanation.

All the intermediates involved in CO<sub>2</sub> reduction reaction on Ni<sub>c</sub>/MgO (110) are shown in Fig. S26-S29. It should be noted that CO formation is not the superior path on Ni(111) and Ni<sub>c</sub>/MgO(110), and adsorption of CO is strong. In addition, CH<sub>2</sub>O\* will be hydrogenated to CH<sub>3</sub>O\* with very low energy rather than desorption (Tables S3-S5), and therefore the selectivity of CO and CH<sub>2</sub>O is low. Since the RDS and selective bifurcation paths on both Ni(111) and Ni<sub>c</sub>/MgO(110) surfaces are similar, a comparison of only the two steps (CH<sub>3</sub>O\*+\*→CH<sub>3</sub>\*+O\* and CH<sub>3</sub>O\*+H\*→CH<sub>3</sub>OH\*+\*) are only required to identify the mechanism on Ni<sub>c</sub>/Al<sub>2</sub>O<sub>3</sub> and Ni<sub>c</sub>/MgAl<sub>2</sub>O<sub>4</sub>. And, the obtained data for these calculations are provided in Table S3-S7. The initial, transition, and final state of CH<sub>3</sub>O\* dissociation on Ni<sub>c</sub>/MgO and Ni<sub>c</sub>/MgAl<sub>2</sub>O<sub>4</sub> are shown in Fig. 5d and e, respectively. The dissociation energy barrier of CH<sub>3</sub>O\* on Ni<sub>c</sub>/Al<sub>2</sub>O<sub>3</sub> is higher than its hydrogenation energy barrier (1.26 and 1.13 eV, respectively), therefore, the high selectivity of CH<sub>4</sub> on Ni/MAO500 may originate due to the presence of Ni<sub>c</sub>/MgO. The CH<sub>3</sub>O\* dissociation energy barrier on Ni<sub>c</sub>/MgAl<sub>2</sub>O<sub>4</sub> is 0.88 eV, which is far lower than 1.45 eV of methanol formation, ensuring the high CH<sub>4</sub> selectivity over the prepared catalysts. However, the low energy barrier can also result in changing the RDS from CH<sub>3</sub>O\* dissociation to HCOOH\* formation (1.00 eV). In Fig. 5c, a direct comparison of the dissociation energy barrier of CH<sub>3</sub>O\* on different catalysts is provided. Accordingly, a significantly reduced energy barrier is obtained for the composite catalysts compared to the bulk Ni catalyst. Besides, not only the activity is improved on the composite surface, the high selectivity of CH<sub>4</sub> is also guaranteed, which is consistent with the experimental results.

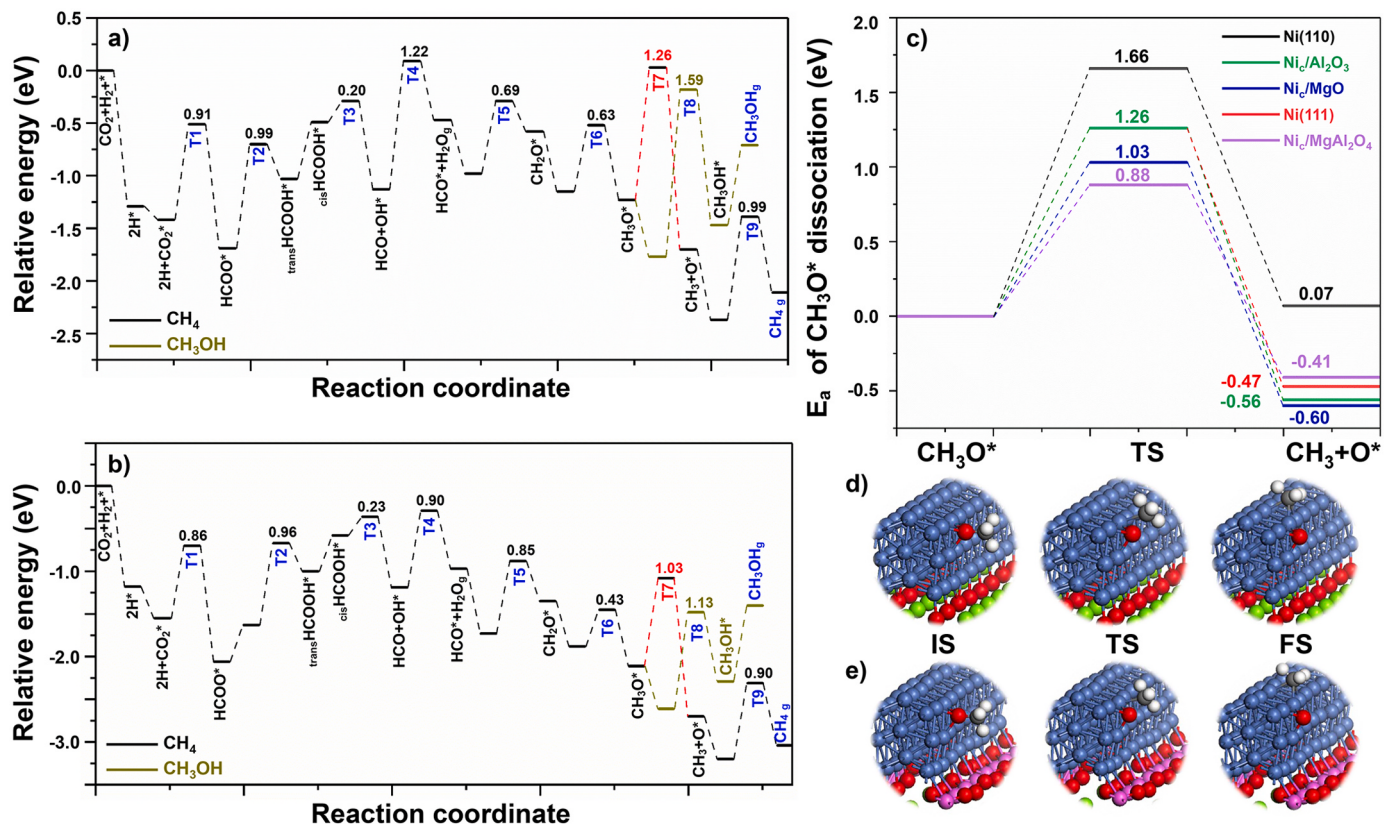


**Fig. 5.** Relative energy diagrams of the optimal formation pathway for CO<sub>2</sub> hydrogenation to CH<sub>4</sub> and CH<sub>3</sub>OH on (a) Ni(111) and (b) Ni<sub>c</sub>/MgO. The red dotted line is the reaction RDS of CH<sub>4</sub> formation. The data labeled on each reaction step in the picture are the energy barrier (E<sub>a</sub>). (c) Comparison of energy barrier of CH<sub>3</sub>O\* dissociation for CH<sub>4</sub> formation on different catalysts. The structures of initial (IS), transition (TS) and final state (FS) of CH<sub>3</sub>O\* dissociation on (d) Ni<sub>c</sub>/MgO and (e) Ni<sub>c</sub>/MgAl<sub>2</sub>O<sub>4</sub>. N<sub>c</sub> stands for Ni cluster.

Therefore, the presence of strong MSI between the substrate (MgAl<sub>2</sub>O<sub>4</sub>) and the Ni cluster, is believed to change the electronic structure of the Ni cluster and then improve the catalytic performance in CO<sub>2</sub> methanation. In general, the different substrates formed upon calcination of the hydrotalcite precursors at different temperatures have different effects. And, the Ni/MAO1000 catalyst with the higher amount of MgAl<sub>2</sub>O<sub>4</sub> showed better catalytic activity than other Ni/MAO catalysts (where their Mg-Al support consisted of MgO and Al<sub>2</sub>O<sub>3</sub> due to the calcination at a lower temperature). Therefore, in general, the obtained experimental as well as DFT results show that the differences in support phase and MSI resulting from thermal treatment have a significant effect on catalytic activity and selectivity.

#### 4. Conclusion

In summary, we prepared a support containing high MgAl<sub>2</sub>O<sub>4</sub> through high-temperature treatment of Mg-Al hydrotalcites, and the thermal tuning MSI is demonstrated. The final catalyst possessed strong MSI between MgAl<sub>2</sub>O<sub>4</sub> and metallic Ni, which therefore led to higher CO<sub>2</sub> methanation activity. More dispersed and smaller Ni particles are achieved if the hydrotalcite precursor is calcined at a higher temperature, and the formed Ni particles can be reduced easily to form Ni(111) plane for H<sub>2</sub> activation and dissociation. Furthermore, the calcination temperature also affected the basic site distribution, and the higher content of weak as well as medium basic sites is responsible for the higher CO<sub>2</sub> adsorption. In-situ DRIFTS results revealed the combination of CO and formate routes during CO<sub>2</sub> methanation, and Ni/MAO1000 with the stronger MSI tended to form more intermediates. DFT calculation results proved that \*CH<sub>3</sub>O dissociation is RDS for methane formation during CO<sub>2</sub> methanation, and the presence of MgAl<sub>2</sub>O<sub>4</sub> phase is

confirmed to be significant for improving CO<sub>2</sub> conversion rate and methane selectivity. Finally, this direct high-temperature treatment of the Mg-Al hydrotalcite significantly increases the MSI and enhances the activity and stability of the catalyst in CO<sub>2</sub> methanation, and the method can potentially be extended to various catalytic reactions using these types of supports.

#### Author contributions

The manuscript was written through contributions of all authors. All authors have given approval to the final version of the manuscript.

#### CRedit authorship contribution statement

**Jie Ren:** Conceptualization, Methodology, Investigation, Formal analysis, Data curation, Writing – original draft, Writing – review & editing, Supervision. **Han Lei:** Methodology, Investigation, Validation, Writing – original draft. **Chalachew Mebrahtu:** Methodology, Writing – review & editing. **Feng Zeng:** Writing – review & editing. **Xusheng Zheng:** Investigation, Writing – review & editing. **Gang Pei:** Writing – review & editing. **Wenhua Zhang:** Conceptualization, Writing – review & editing, Supervision. **Zhandong Wang:** Writing – review & editing, Funding acquisition, Supervision.

#### Declaration of Competing Interest

The authors declare no competing interests.

## Data Availability

Data will be made available on request.

## Acknowledgments

This work was funded by the National Key Research and Development Program of China (2019YFA0405602), the Hefei Science Center, CAS (2020HSC-KPRD001, 2021HSC-UE005), the DNL Cooperation Fund, CAS (DNL202005) and CAS Project for Young Scientists in Basic Research (YSBR-051). Besides, we would like to thank Dr. Hongliang Li at the University of Science and Technology of China for valuable suggestions, and the help with sXAS characterization of the photoemission end stations (BL10B) in National Synchrotron Radiation Laboratory (NSRL). All the calculations were performed on the supercomputing center of the University of Science and Technology of China (USTC-SCC).

## Appendix A. Supporting information

Supplementary data associated with this article can be found in the online version at [doi:10.1016/j.apcatb.2023.123245](https://doi.org/10.1016/j.apcatb.2023.123245).

## References

- [1] S.R. Foit, I.C. Vinke, L.G.J. deHaart, R.A. Eichel, *Angew. Chem. Int. Ed.* **56** (2017) 5402–5411.
- [2] J. Ren, J.P. Cao, X.Y. Zhao, Y.L. Liu, *Chem. Eng. J.* **429** (2022) 132316–132341.
- [3] F. Wang, S. He, H. Chen, B. Wang, L. Zheng, M. Wei, D.G. Evans, X. Duan, *J. Am. Chem. Soc.* **138** (2016) 6298–6305.
- [4] J. Ren, C. Mebrahtu, L. van Koppen, F. Martinovic, J.P. Hofmann, E.J.M. Hensen, R. Palkovits, *Chem. Eng. J.* **426** (2021) 131760–131775.
- [5] F. He, J. Zhuang, B. Lu, X. Liu, J. Zhang, F. Gu, M. Zhu, J. Xu, Z. Zhong, G. Xu, F. Su, *Appl. Catal. B-Environ.* **293** (2021), 120218–120233.
- [6] L. Shen, J. Xu, M. Zhu, Y.F. Han, *A.C.S. Catal.* **10** (2020) 14581–14591.
- [7] J. Ren, H. Lou, N. Xu, F. Zeng, G. Pei, Z. Wang, *J. Energy Chem.* **80** (2023) 182–206.
- [8] Z. Liu, X. Gao, B. Liu, Q. Ma, T.S. Zhao, J. Zhang, *Fuel* **321** (2022) 124115–124128.
- [9] N. Bette, J. Thielemann, M. Schreiner, F. Mertens, *ChemCatChem* **8** (2016) 2903–2906.
- [10] J. Ren, Y.L. Liu, *Appl. Catal. B-Environ.* **300** (2022) 120743–120758.
- [11] S. Abate, K. Barbera, E. Giglio, F. Deorsola, S. Bensaid, S. Perathoner, R. Pirone, G. Centi, *Ind. Eng. Chem. Res.* **55** (2016) 8299–8308.
- [12] J. Ren, C. Mebrahtu, R. Palkovits, *Catal. Sci. Technol.* **10** (2020) 1902–1913.
- [13] C.T. Campbell, *Nat. Chem.* **4** (2012) 597–598.
- [14] T.W. van Deelen, C. Hernández Mejía, K.P. de Jong, *Nat. Catal.* **2** (2019) 955–970.
- [15] S. Chen, A.M. Abdel-Mageed, M. Li, S. Cisneros, J. Bansmann, J. Rabieah, A. Brückner, A. Groß, R.J. Behm, *J. Catal.* **400** (2021) 407–420.
- [16] S. Lin, Z. Hao, J. Shen, X. Chang, S. Huang, M. Li, X. Ma, *J. Energy Chem.* **59** (2021) 334–342.
- [17] A. Parastaev, V. Muravev, E. Huertas Osta, A.J.F. van Hoof, T.F. Kimpel, N. Kosinov, E.J.M. Hensen, *Nat. Catal.* **3** (2020) 526–533.
- [18] T. Pu, J. Chen, W. Tu, J. Xu, Y.F. Han, I.E. Wachs, M. Zhu, *J. Catal.* **413** (2022) 821–828.
- [19] L.L. Shen, K. Xia, W.Z. Lang, L.F. Chu, X. Yan, Y.J. Guo, *Chem. Eng. J.* **324** (2017) 336–346.
- [20] G. Kresse, J. Furthmüller, *Comput. Mater. Sci.* **6** (1996) 15–50.
- [21] P.E. Blöchl, *Phys. Rev. B* **50** (1994) 17953–17979.
- [22] J.P. Perdew, K. Burke, M. Ernzerhof, *Phys. Rev. Lett.* **77** (1996) 3865–3868.
- [23] H.J. Monkhorst, J.D. Pack, *Phys. Rev. B* **13** (1976) 5188–5192.
- [24] S. Grimme, *J. Comput. Chem.* **27** (2006) 1787–1799.
- [25] C.C. Tran, O. Mohan, A. Banerjee, S.H. Mushrif, S. Kaliaguine, *Energy Fuels* **34** (2020) 16265–16273.
- [26] G. Henkelman, B.P. Uberuaga, H. Jónsson, *113*, 2000, pp. 9901–9904.
- [27] K. Xia, W.Z. Lang, P.P. Li, L.L. Long, X. Yan, Y.J. Guo, *Chem. Eng. J.* **284** (2016) 1068–1079.
- [28] Y. Lou, J. Xu, Y. Zhang, C. Pan, Y. Dong, Y. Zhu, *Mater. Today Nano* **12** (2020) 100093–100116.
- [29] M. Zeng, L. Cheng, Q. Gu, B. Yang, B. Yu, J. Xu, Y. Zhang, C. Pan, X.-M. Cao, Y. Lou, Y. Zhu, *E.E.S. Catalysis* **1** (2023) 153–161.
- [30] S. Li, Y. Xu, Y. Chen, W. Li, L. Lin, M. Li, Y. Deng, X. Wang, B. Ge, C. Yang, S. Yao, J. Xie, Y. Li, X. Liu, D. Ma, *Angew. Chem. Int. Ed.* **56** (2017) 10761–10765.
- [31] T. Abe, M. Tanizawa, K. Watanabe, A. Taguchi, *Energy Environ. Sci.* **2** (2009) 315–321.
- [32] M. Roiaz, E. Monachino, C. Dri, M. Greiner, A. Knop-Gericke, R. Schlägl, G. Comelli, E. Vesselli, *J. Am. Chem. Soc.* **138** (2016) 4146–4154.
- [33] E.B. Sterk, A.E. Nieuwinkel, M. Monai, J.N. Louwen, E.T.C. Vogt, I.A.W. Filot, B. M. Weckhuysen, *J.A.C.S. Au*, *J.A.C.S. Au* **2** (2022) 2714–2730.
- [34] J. Ren, F. Zeng, C. Mebrahtu, Z. Wang, R. Palkovits, *J. Energy Chem.* (2023), <https://doi.org/10.1016/j.jecchem.2023.07.017>.
- [35] J. Tian, P. Zheng, T. Zhang, Z. Han, W. Xu, F. Gu, F. Wang, Z. Zhang, Z. Zhong, F. Su, G. Xu, *Appl. Catal. B-Environ.* **339** (2023), 123121.
- [36] D. Liang, Y. Wang, M. Chen, X. Xie, C. Li, J. Wang, L. Yuan, *Appl. Catal. B-Environ.* **322** (2023), 122088.
- [37] Y. Cheng, D. Zheng, W. Xu, H. Geng, X. Lu, *J. Mater. Chem. A* **8** (2020) 17741–17746.
- [38] Y. Shi, Y. Zhou, Y. Lou, Z. Chen, H. Xiong, Y. Zhu, *Adv. Sci.* **9** (2022) 2201520–2201560.
- [39] Y. Lou, F. Jiang, W. Zhu, L. Wang, T. Yao, S. Wang, B. Yang, B. Yang, Y. Zhu, X. Liu, *Appl. Catal. B-Environ.* **291** (2021) 120122–120129.
- [40] A. Solis-Garcia, J.F. Louvier-Hernandez, A. Almendarez-Camarillo, J.C. Fierro-Gonzalez, *Appl. Catal. B-Environ.* **218** (2017) 611–620.
- [41] W.L. Vrijburg, E. Moioli, W. Chen, M. Zhang, B.J.P. Terlingen, B. Zijlstra, I.A. W. Filot, A. Züttel, E.A. Pidko, E.J.M. Hensen, *ACS Catal.* **9** (2019) 7823–7839.
- [42] C. Vogt, E. Groeneveld, G. Kamsma, M. Nachtegaal, L. Lu, C.J. Kiely, P.H. Berben, F. Meirer, B.M. Weckhuysen, *Nat. Catal.* **1** (2018) 127–134.
- [43] H. Muroyama, Y. Tsuda, T. Asakoshi, H. Misatoh, T. Okanishi, T. Matsui, K. Eguchi, *J. Catal.*, *J. Catal.* **343** (2016) 178–184.
- [44] X. Jia, X. Zhang, N. Rui, X. Hu, C.J. Liu, *Appl. Catal. B-Environ.* **244** (2019) 159–169.
- [45] J.J.C. Struijs, V. Muravev, M.A. Verheijen, E.J.M. Hensen, N. Kosinov, *Angew. Chem. Int. Ed.* **62** (2023), e202214864.
- [46] X. Xu, L. Liu, Y. Tong, X. Fang, J. Xu, D.E. Jiang, X. Wang, *ACS Catal.* **11** (2021) 5762–5775.
- [47] Y. Xie, J. Chen, X. Wu, J. Wen, R. Zhao, Z. Li, G. Tian, Q. Zhang, P. Ning, J. Hao, *ACS Catal.* **12** (2022) 10587–10602.
- [48] F. Hu, R. Ye, C. Jin, D. Liu, X. Chen, C. Li, K.H. Lim, G. Song, T. Wang, G. Feng, R. Zhang, S. Kawi, *Appl. Catal. B-Environ.* **317** (2022) 121715–121725.
- [49] J. Ren, F. Zeng, C. Mebrahtu, R. Palkovits, *J. Catal.* **405** (2022) 385–390.